JGR Atmospheres

RESEARCH ARTICLE
10.1029/2025JD045882

Nationwide Overestimation of Black Carbon Emissions During Clean Air Action Identified by Assimilation Inversion

Li Fang[1], Jianbing Jin[1], Jiandong Wang[2], Kang Hu[1], Nan Li[1], Mijie Pang[3], and Hong Liao[1]

[1]State Key Laboratory of Climate System Prediction and Risk Management, Jiangsu Key Laboratory of Atmospheric Environment Monitoring and Pollution Control, Jiangsu Collaborative Innovation Center of Atmospheric Environment and Equipment Technology, School of Environmental Science and Engineering, Nanjing University of Information Science and Technology, Nanjing, China, [2]School of Atmospheric Physics, Nanjing University of Information Science and Technology, Nanjing, China, [3]Delft Institute of Applied Mathematics, Delft University of Technology, Delft, The Netherlands

Abstract An accurate estimate of black carbon (BC) emission is critical, as BC represents one of the most important short-lived climate forcers. The widely used BC emission inventories were developed using either bottom-up or top-down approaches, both of which have large uncertainties. The challenges of the bottom-up approach include uncertainties in emission factors for different fuel types and combustion technologies. Conversely, top-down BC emission inversion relies primarily on satellite-retrieved aerosol absorption optical depth, which has significant limitations in quantifying BC-specific contributions. The China Atmospheric Monitoring Network, established by the China Meteorological Administration, provides ground-based hourly BC observations and a valuable opportunity to constrain BC emissions. This study presents the first application of these nationwide BC observations in emission inversion during the Clean Air Action (2013–2017), achieved using the 4DEnVar assimilation technique. Validation against independent observations demonstrates significant improvements in posterior estimates, reducing the root mean square error by 36.7%. Compared to the posterior, widely used bottom-up inventories (e.g., MEIC) overestimate China's total BC emissions by 36.7%, with overestimations ranging up to 80.6% in the North China Plain (averaged between 2013 and 2017). In terms of climate impact, MEIC-based estimates yield an 18.7% higher direct radiative effect on average, while CMIP6 historical estimates further exaggerate BC-induced forcing by a factor of 1.7. Additionally, our inversion reveals that annual total BC emissions declined markedly by 28.1% during the Clean Air Action, from 1.24 to 0.89 Tg. These findings are critical for quantifying the role of BC in the regional and global climate.

Plain Language Summary Black carbon (BC), or soot, is one of the major contributors to climate warming. However, scientists have struggled to accurately measure how much BC is released into the atmosphere. Traditional estimation methods either rely on calculations based on fuel use and combustion technology (which are highly uncertain) or on satellite measurements (which can't reliably distinguish BC from other pollutants). This study takes a new approach by using data from ground-based monitoring stations across China that directly measure BC in the air every hour. We applied these measurements to improve emission estimates during China's Clean Air Action period (2013–2017). Our results show that previous estimates significantly overestimated BC emissions in China by 36.7% on average, and by as much as 80.6% in some regions like the North China Plain. These overestimates led to inflated calculations of BC's warming effect on the climate, with some estimates being 1.7 times higher than reality. We also found that China's BC emissions dropped dramatically by 28.1% during the 5-year Clean Air Action, falling from 1.24 to 0.89 million metric tons annually. These more accurate measurements are essential for understanding BC's true role in regional and global climate change.

Key Points:

- MEIC overestimated China's black carbon emissions by 36.7%
- BC's climate warming effect in CMIP6 was overstated by up to 75.7%
- China's BC emissions declined 28.1% during the Clean Air Action from 2013 to 2017

Supporting Information:

Supporting Information may be found in the online version of this article.

Correspondence to:

J. Jin and H. Liao,
jianbing.jin@nuist.edu.cn;
hongliao@nuist.edu.cn

Citation:

Fang, L., Jin, J., Wang, J., Hu, K., Li, N., Pang, M., & Liao, H. (2026). Nationwide overestimation of black carbon emissions during clean air action identified by assimilation inversion. *Journal of Geophysical Research: Atmospheres*, *131*, e2025JD045882. https://doi.org/10.1029/2025JD045882

Received 18 NOV 2025
Accepted 16 FEB 2026

Author Contributions:

Conceptualization: Li Fang, Jianbing Jin, Hong Liao
Data curation: Kang Hu, Nan Li
Formal analysis: Li Fang
Funding acquisition: Jianbing Jin, Hong Liao
Investigation: Jiandong Wang
Methodology: Li Fang, Jianbing Jin
Project administration: Jianbing Jin, Hong Liao
Resources: Jiandong Wang, Kang Hu, Nan Li, Mijie Pang
Supervision: Jianbing Jin, Hong Liao
Validation: Li Fang, Mijie Pang
Visualization: Li Fang, Jianbing Jin
Writing – original draft: Li Fang
Writing – review & editing: Jianbing Jin, Jiandong Wang, Hong Liao

1. Introduction

Atmospheric aerosols play a crucial role in the Earth's climate system by directly scattering and absorbing solar radiation (McCormick & Ludwig, 1967; Schulz et al., 2006) and indirectly influencing cloud properties and precipitation processes (Andreae & Rosenfeld, 2008; Rosenfeld, 2000). Among them, black carbon (BC)—a light-absorbing carbonaceous aerosol emitted primarily from incomplete combustion—has attracted growing attention due to its complex interactions with climate and air quality (Bond et al., 2004). It is a specific pollutant

that can influence the development of the boundary layer by altering the atmospheric heating rate, thus worsening air pollution (A. J. Ding et al., 2016; J. Wang et al., 2023). Additionally, BC is an effective short-lived climate forcer (Ramanathan & Carmichael, 2008), directly absorbing incoming shortwave solar radiation (Liousse et al., 1993; Menon et al., 2002), which contributes to climate warming. According to the latest IPCC Sixth Assessment Report, the effective radiative forcing of BC is estimated to range from −0.28 to 0.41 W m^{-2}, contributing to a temperature increase of 0.1°C between 1750 and 2019 (Dentener et al., 2021). BC emissions and their climatic impacts are also a key focus of global climate modeling frameworks, including the Coupled Model Intercomparison Project Phase 6 (CMIP6) (Eyring et al., 2016). A clear understanding of the spatial and temporal distribution of BC emissions is crucial to address its environmental and climatic impacts.

Despite its significance, BC emission estimates are subject to substantial uncertainties (Bond et al., 2004; H. Xu et al., 2021). Traditional BC emission inventories are generally constructed using a bottom-up approach based on emission source intensity data and emission factors (EFs), which, however, vary significantly across regions, fuel types, and combustion technologies (Cao et al., 2006; Paliwal et al., 2016; Penner et al., 1993). For instance, the EFs for BC from passenger cars can vary by orders of magnitude depending on vehicle type, fuel quality, and combustion efficiency (Karavalakis et al., 2014). The residential sector also contributes significant uncertainty due to a lack of detailed fuel consumption data and the diverse energy-use patterns across rural and urban households (W. Zhang et al., 2018). As highlighted by Tao et al. (2018), residential energy use in rural China has undergone rapid changes, deviating notably from official statistics in both magnitude and trends. Furthermore, the update of emission inventories often has a significant lag, reducing their utility for timely policy applications.

Alongside the bottom-up approach, the top-down method for emission estimation is also widely favored. With the rapid surge in satellite observations, attempts have been made to assimilate satellite measurements of aerosol optical depth (AOD) (Huneeus et al., 2013; X. Xu et al., 2013) or aerosol absorption optical depth (AAOD) (L. Zhang et al., 2015; C. Chen et al., 2019; Zhao et al., 2024) into models to refine BC emission estimates. However, AAOD, which quantifies the absorbing component of AOD, is recognized to be more uncertain than AOD itself (Schutgens et al., 2021). Additionally, AAOD encompasses absorbing aerosol species such as organic carbon, BC, and mineral dust (Kinne et al., 2006), making it challenging to isolate and accurately estimate BC-specific AAOD (BC-AAOD) from the total AAOD. Consequently, these optimizations cannot be regarded as being specifically tailored to BC, and significant uncertainties persist in their representation.

Ground-based and airborne observations are believed to be more reliable, for example, the Aethalometer AE-31 measurements have fewer uncertainties than satellite observations because they directly measure BC at ground level with minimal atmospheric interference, avoiding the complex retrieval algorithms, cloud contamination, surface reflectance effects, and vertical column integration uncertainties (X. Wang et al., 2016). Several studies have highlighted the effectiveness of advanced data assimilation techniques in enhancing the accuracy of BC emission estimates with these measurements. For instance, Hakami et al. (2005) used an adjoint model with the four-dimensional variational data assimilation (4D-Var) approach during the Asian Pacific Regional Aerosol Characterization Experiment in April 2001. This method effectively optimized BC emissions and conditions, resulting in considerable regional adjustments in anthropogenic emissions, particularly a reduction in south-eastern China and increases in northeast China and Japan. Utilizing ground BC observations from 42 stations in eastern and northern China, Jia et al. (2021) applied the Bayesian inversion framework to investigate changes in BC emissions in China during the 2020 Spring Festival. BC was measured with a field semi-online OC/EC analyzer with a $PM_{2.5}$ cyclone inlet (Sunset Laboratory Inc., USA). Their results indicated reductions of 70% in eastern China and 48% in northern China in BC emissions. These studies primarily rely on in situ measurements or airborne observations, which offer precise data on aerosol properties. However, they frequently exhibit limited spatial and temporal coverage due to the constrained observational data sets.

China is one of the major anthropogenic BC source regions in the world, with its BC emissions growing by 21% from 1996 to 2010 (Lu et al., 2011). Thanks to the implementation of the Clean Air Action Plan from 2013 to 2017 (China's first 5-year plan), China has achieved great success in reducing $PM_{2.5}$ levels (State Council of the People's Republic of China, 2018). However, understanding of the long-term variations in BC and its radiative effects in response to the “Atmospheric Pollution Prevention and Control Action Plan” is still insufficient (Sun et al., 2022). Studies on BC emission inversion focusing on China are minimal, especially those involving long-term emission inversion. L. Zhang et al. (2015) utilized the 4D-Var data assimilation technique to inverse BC emissions by assimilating the Ozone Monitoring Instrument (OMI) observations of AAOD with the GEOS-Chem

adjoint model for April and October 2006. The results showed that correlations between OMI AAOD and GEOS-Chem–simulated AAOD were weak for both the prior and posterior emission estimates, and assimilating satellite AAOD yielded only limited improvement. Using an ensemble optimal interpolation with ground BC observations, P. Wang et al. (2016) inverted monthly 2008 BC emissions, finding systematic underestimation in prior inventories and achieving a nearly 30% reduction in the average root mean square error (RMSE) of simulated daily BC. Recently, Zhao et al. (2024) developed an AAOD–ML–inversion framework for China (2000–2020), in which the OMI AAOD product was first gap-filled by learning from the Modern-Era Retrospective Analysis for Research and Applications Version 2 (MERRA-2) AAOD fields, and the BC-AAOD component was subsequently separated using BC fraction coefficients from MERRA-2. The resulting gridded OMI BC-AAOD data were then employed to constrain BC emissions through the CMAQ top-down inversion system. However, it should be noted that the MERRA-2 AAOD reanalysis is a diagnostic variable, derived solely from the assimilation of AOD observations combined with prior information from the GEOS-5/GOCART aerosol model. Its accuracy strongly depends on the simulated aerosol concentration ratios, physical parameters (e.g., particle radius), and optical properties from the prior GEOS-5/GOCART simulation (Randles et al., 2017; J. Jin, Lin, et al., 2019). Therefore, reliance on empirically derived MERRA-2 AAOD and BC fractions may misrepresent the true BC contribution and propagate bias into the emission inversion. Those abovementioned studies either estimated BC emissions indirectly by assimilating AAOD or focused primarily on emission inventories prior to 2010. To the best of our knowledge, a long-term inversion of BC emissions in China based on ground-based BC observations for the period 2013–2017 has not yet been conducted.

Fortunately, the China Atmospheric Monitoring Network has made long-term ground BC observations available, with a total of 42 sites covering the Clean Air Action Plan period (Guo et al., 2020). This extensive data set enables us to make long-term BC emission inversion. This study presents a BC emission estimation in China ranging from 2013 to 2017, using ground BC measurements and the GEOS-Chem model. The emission inversion is conducted based on a four-dimensional ensemble variational (4DEnVar) data assimilation algorithm. Independent BC observations collected from various public papers and data sets are utilized for evaluating the strengths of inversion. Satellite AAOD data are also collected to examine the improvements from our posterior emission inventory. The spatial characteristics of BC distribution, the temporal variation, and the total emission changes during the Clean Air Action Plan will be reevaluated based on the updated BC emission inventory. The direct radiative effect (DRE) in response to BC emission changes will also be investigated. This will facilitate a more informed assessment of climate responses to projected future emissions.

2. Materials and Methods

This section introduces the data and methods as follows: Section 2.1 outlines the study domain and describes the two BC ground observation data sets used for data assimilation and independent validation. Section 2.2 introduces the satellite AAOD sources and processing methods for validation as well. Section 2.3 details the GEOS-Chem model configuration, and Section 2.4 describes the prior BC emission inventories. Section 2.5 presents the emission inversion system based on the 4DEnVar framework.

2.1. Study Domain and Ground Observations

The study period encompasses the entire duration of the Clean Air Action Plan, spanning from 2013 to 2017. Two data sets of ground BC observations during this period were collected. The first data set (hereinafter referred to as Data set 1) originates from the long-term in situ observations of the China Atmospheric Monitoring Network (Y. Zhang et al., 2019; Guo et al., 2020), and these BC measurements are used for data assimilation. The distribution of observation sites (Data set 1) and the amount of valid data at each location during the study period are illustrated in Figure 1. The second data set (hereinafter referred to as Data set 2) was collected from various publicly available papers and open data sources. It serves as an independent validation data set, with detailed sources provided in Table S1 in Supporting Information S1. The four primary megacity clusters, which are more developed, are discussed in greater detail. These include the North China Plain (NCP; 34–41° N, 113–119° E), the Yangtze River Delta (YRD; 30–33° N, 119–122° E), the Pearl River Delta (PRD; 21.5–24° N, 112–115.5° E), and the Sichuan Basin (SCB; 28.5–31.5° N, 103.5–107° E). They are represented by black boxes in Figure 1.

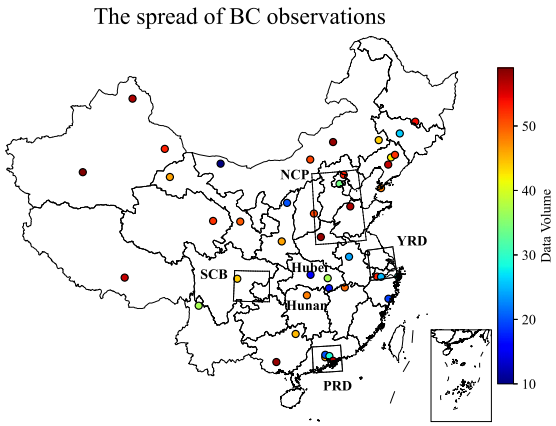

Figure 1. The spatial distribution of BC ground observation sites (Data set 1) and the volume of effective data (represented by colors) at each site from 2013 to 2017. Black rectangles represent the four primary megacity clusters in the study area.

2.2. OMI AAOD

The AAOD data are derived from OMI/Aura Near UV Aerosol Optical Depth product (OMAERUVd) in GES DISC (Torres, 2008). It is a Level-3 daily global gridded data set (1° × 1° latitude/longitude resolution) generated by the OMI science team through quality filtering and spatial averaging of Level-2 OMAERUV orbital data. The OMI instrument aboard NASA's Aura satellite provides observations with a spatial resolution of 13 × 24 km at nadir. The OMAERUV retrieval algorithm is based on the enhanced TOMS version-8 algorithm, which utilizes ultraviolet radiance measurements to derive aerosol properties, and the product contains both extinction and absorption optical depths at three wavelengths: 355, 388, and 500 nm. The near-UV retrieval approach offers distinct advantages for aerosol characterization, including high sensitivity to absorbing aerosols and low surface albedo in the near-UV spectrum, enabling aerosol retrievals over bright surfaces such as deserts where visible-wavelength algorithms often struggle.

The absorption aerosol optical depth at 550 nm ($AAOD_{550}$) was derived through spectral interpolation using the Ångström exponent approach, a widely accepted method for estimating aerosol optical properties at intermediate wavelengths. The Ångström power law describes how aerosol optical thickness varies with wavelength, enabling calculation of optical depth at unmeasured wavelengths when measurements at two reference wavelengths are available. In this study, the Ångström exponent (β) was first computed from the ratio of AAOD measurements at 388 and 500 nm using the logarithmic relationship:

$$\beta = -\frac{\ln(AAOD_{388}/AAOD_{500})}{\ln(388/500)}. \quad (1)$$

Subsequently, $AAOD_{550}$ was extrapolated from the 500 nm measurement according to the power law relationship:

$$AAOD_{550} = AAOD_{500}\left(\frac{550}{500}\right)^{-\beta}. \quad (2)$$

This interpolation method has been extensively validated in aerosol remote sensing applications (Cesnulyte et al., 2014; J. Jin, Segers, et al., 2019). It provides reliable estimates when the spectral dependence of aerosol properties remains relatively stable across the wavelength range of interest. The interpolated $AAOD_{550}$ was further interpolated onto the GEOS-Chem simulation grids for comparison.

2.3. Model Description

In this study, we utilized the GEOS-Chem chemical transport model (version 13.4.0) obtained from Zenodo (The International GEOS-Chem User Community, 2022). The model's simulations were driven by meteorological fields from NASA's Global Modeling and Assimilation Office, specifically using the MERRA-2 data set as described by (Gelaro et al., 2017). The model incorporates a comprehensive chemical mechanism that includes interactions between aerosols, ozone, NOx, and hydrocarbons (Park et al., 2004). We applied a global configuration with a coarse resolution of 2° latitude × 2.5° longitude to establish boundary conditions. Within the study's focus area, the nested domain (0–55°N, 70–140°E) was simulated with a finer spatial resolution of 0.5° latitude × 0.625° longitude and utilized 47 vertical layers. The representation of BC in the GEOS-Chem model follows Park et al. (2003). In this framework, BC is modeled using two tracers: hydrophobic and hydrophilic BC. Upon emission, 80% of BC is initially assumed to be hydrophobic, transitioning to a hydrophilic state with an e-folding timescale of 1.15 days (Cooke et al., 1999; Park et al., 2005).

The Rapid Radiative Transfer Model for GCMs (RRTMG) has been integrated online with the GEOS-Chem model, following the methodology detailed by Heald et al. (2014). This model computes radiative transfer across 14 shortwave and 16 longwave spectral bands, spanning wavelengths from 230 nm to 56 μm (Iacono

et al., 2008). To capture the radiative effects, instantaneous fluxes are calculated every 3 hr for both shortwave and longwave radiation. In this study, the GEOS-Chem simulated AAOD is the sum of BC-AAOD, OC-AAOD, and dust-AAOD. The DRE of BC at the top of the atmosphere (TOA) is derived from the clear-sky shortwave radiation outputs generated by RRTMG.

2.4. Emission Inventory

The global anthropogenic BC emissions utilized in this study are sourced from the Community Emissions Data System (CEDS) inventory (v_2021_04_21), which includes a wide range of aerosols, aerosol precursors, and reactive compounds (Hoesly et al., 2018). Global biomass burning emissions are derived from the Global Fire Emissions Database, version 4 (GFED4; (Giglio et al., 2013)). For the China region, anthropogenic emissions were adjusted using the Multi-resolution Emission Inventory for China (MEIC) (Li et al., 2017). It should be noted that anthropogenic emissions account for over 99% of BC sources in China, as reported by Lu et al. (2011). The MEIC serves as the primary prior BC emission inventory in this study and will be compared with the posterior emission estimates. Additionally, the anthropogenic emission data set of CMIP6 (Feng et al., 2020) was applied when simulating the CMIP6 scenario for comparison. Since the historical data extend only until 2014, simulations under this scenario were limited to the years 2013 and 2014. Due to their minimal contributions, emissions from aircraft and shipping were not considered in this study.

2.5. Emission Inversion Methodology

In this study, we utilize the 4DEnVar data assimilation technique to perform BC emission inversion, which was developed in our previous work (J. Jin et al., 2023). One of the key advantages of the 4DEnVar approach, compared to traditional four-dimensional data assimilation methods, is that it circumvents the requirement for tangent linear and adjoint models during both the formulation and implementation phases (Liu et al., 2008). The fundamental concept of emission inversion through data assimilation is to determine the most probable estimate of the monthly BC emissions $\vec{f}$, based on a combination of prior emissions and observational data. This estimate is obtained by minimizing the cost function $\mathcal{J}$:

$$\mathcal{J}(\vec{f}) = \frac{1}{2}(\vec{f}-\vec{f}_b)^{\mathrm{T}}\mathbf{B}^{-1}(\vec{f}-\vec{f}_b) + \frac{1}{2}\{\vec{y}-\mathbf{H}\mathcal{M}(\vec{f})\}^{\mathrm{T}}\mathbf{O}^{-1}\{\vec{y}-\mathbf{H}\mathcal{M}(\vec{f})\}, \quad (3)$$

here, $\vec{f}_b$ denotes the prior vector for monthly BC emissions, while $\mathbf{B}$ is the background error covariance matrix associated with this prior estimate. The operator $\mathcal{M}$ represents the GEOS-Chem model, and $\mathbf{H}$ is the observational operator that transfers the simulated BC concentrations into the observational space. The vector $\vec{y}$ corresponds to the monthly ground-based BC measurements, with $\mathbf{O}$ serving as the observation error covariance matrix. Since we assume that the BC observations are independent of one another, $\mathbf{O}$ is represented as a diagonal matrix, with its entries reflecting the uncertainties associated with each observation. Here, we adopt a strong-constraint variational assimilation framework in which the forward model is assumed perfect over the assimilation window, and emissions are the only optimized control variables. Consequently, uncertainties in meteorology/transport (e.g., boundary-layer mixing) and aerosol processes (e.g., deposition and aging) are not corrected explicitly; their effects instead contribute to the residual observation–model mismatch in Equation 3 together with the prescribed observation-error statistics. The posterior emissions should therefore be interpreted as the most probable estimate conditional on the GEOS-Chem model and assumed error characteristics.

In this study, the diagonal elements of $\mathbf{O}$ are intended to represent the total uncertainty associated with each monthly mean ground-based BC observation, that is, the uncertainty used to weight the mismatch between a point measurement and the corresponding model grid-cell monthly mean. We treated $\mathbf{O}$ as diagonal since the assimilated BC observations were collected independently. Given the limited and spatially uneven surface network, we do not attempt to explicitly parameterize additional representativeness errors associated with unresolved sub-grid spatial heterogeneity. The uncertainty assigned to each monthly observation is estimated from the standard deviation of daily mean BC concentrations within that month, which provides a practical measure of month-scale variability and sampling uncertainty in the aggregated monthly mean used in the inversion.

We assume that uncertainties in BC emissions can be represented by a spatially varying scaling factor, α. The value of α is treated as a random variable with a mean of 1.0 and a standard deviation of $\sigma_\alpha = 0.2$. Additionally, a

correlation matrix **C** is employed to quantify the spatial correlation between the scaling factors at different grid cells, i and j. This correlation is defined as:

$$\mathbf{C}(i,j) = e^{-(d_{i,j}/l)^2/2}, \tag{4}$$

where $d_{i,j}$ denotes the distance between grid cells i and j, and l is the correlation length scale that controls the spatial smoothness of the scaling factors. A smaller value of l allows the assimilation process to resolve finer-scale errors, although it requires a larger ensemble size to adequately capture the emission-to-simulation variability. We tested l values of 200, 300, and 400 km and found that a smaller l allows more localized adjustments but can yield noisier increments under limited ensemble size and uneven observational coverage, whereas a larger l tends to oversmooth spatial gradients and weakens the correction of regional mismatches (J. Jin et al., 2023). With 16 ensemble members, $l = 300$ km provides the best performance against independent observations (Data set 2) and is therefore adopted. Note that the correlation scale can vary regionally (e.g., more localized in urban source regions). A single, domain-wide l is a pragmatic regularization choice given the monthly inversion framework and the available observational density, and that spatially varying correlation structures will be explored in future work. Using the spatial correlation matrix, we construct the background error covariance matrix for the scaling factor, $\mathbf{B}_\alpha$, as follows:

$$\mathbf{B}_\alpha(i,j) = \sigma_\alpha \cdot \mathbf{C}(i,j), \tag{5}$$

Subsequently, the background error covariance matrix for BC emissions, denoted as **B**, is computed using element-wise multiplication:

$$\mathbf{B} = \mathbf{B}_\alpha \circ \mathbf{C}, \tag{6}$$

In this study, an ensemble size of 16 is employed to construct the background error covariance. The optimized BC emissions, $\vec{f}$, are obtained by minimizing the cost function defined earlier through the 4DEnVar process, with detailed procedures described in J. Jin et al. (2023). Note that although BC measurements are available at hourly resolution, $\vec{y}$ is constructed from monthly mean surface BC concentrations, and $\vec{f}$ represents monthly emissions. This temporal aggregation reduces sensitivity to sub-monthly meteorological variability (e.g., day-to-day PBL fluctuations) and strengthens the month-scale emission constraint.

The inversion seeks the maximum a posteriori emission estimate by minimizing the Bayesian cost function (Equation 3). The relative influence of the prior emissions and the observations is determined by the prescribed error covariance matrices **B** and **O**: departures from the prior are penalized according to **B**, while observation–model mismatches are weighted by **O**. Consequently, emission updates occur only when supported by observational information strong enough to overcome the regularization imposed by the prior term. A limitation of the strong-constraint inversion is that uncertainties in transport, mixing, and deposition are not explicitly estimated, and persistent model-process biases may therefore influence the inferred posterior emissions. A weak-constraint formulation, in which model error terms (or bias/process parameters) are included in the control vector, could provide a more balanced partitioning between emission errors and model/process errors in certain regimes (Babyale et al., 2025). However, implementing weak-constraint assimilation at the present scale would substantially increase computational cost, and is left for future work.

3. Results

This section presents the main results and discussion as follows: Section 3.1 evaluates the GEOS-Chem simulations and emission inversion by comparing model results with ground-based BC observations and satellite AAOD, and analyzes the spatial and temporal distributions of BC surface concentrations. Section 3.2 examines the spatiotemporal variations in BC emissions, highlighting key differences among the prior, posterior, and CMIP6 historical inventories. Section 3.3 discusses the BC DRE at the TOA and its temporal trends during the Clean Air Action Plan period.

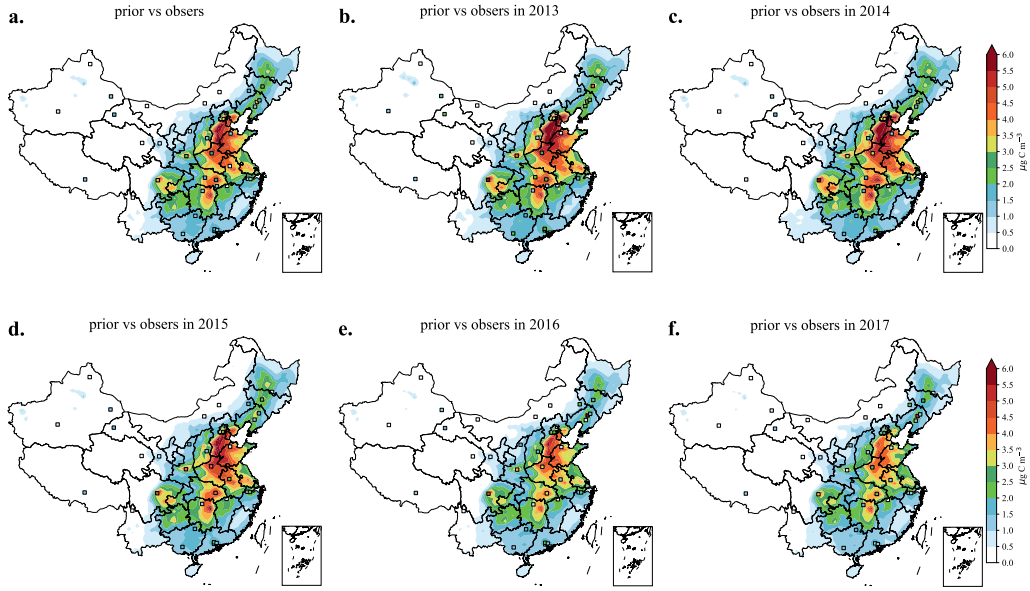

Figure 2. The spatial distribution of BC simulations and the BC ground observations from Data set 1. Panel (a) shows the average results over the entire five-year period, while Panels (b)–(f) depict the annual averages for each year from 2013 to 2017, respectively.

3.1. Emission Inversion Validation

The performance of GEOS-Chem simulations was evaluated by comparing monthly ground BC simulations with ground-based BC observations from Data set 1. Figure 2a implies that GEOS-Chem simulations tend to overestimate BC concentrations in eastern and central China, particularly over NCP, YRD, Hubei province, and Hunan province. Statistically, the RMSE, mean absolute error (MAE) and normalized mean bias (NMB) during the 5-year period in the four major megacity clusters were 2.67 μg C m^{-3}, 1.84 μg C m^{-3}, and +45.94%, respectively. These metrics indicate that while the model captures the overall spatiotemporal patterns of ground-based BC observations to some extent, discrepancies remain. Similar trends in overestimation are corroborated by the results presented in Figure 4a, based on an independent data set.

The posterior BC emission estimates, derived by assimilating ground-based BC observations from Data set 1, significantly improve GEOS-Chem simulation accuracy when used as input. It should be noted that Data set 1 observations were processed using AE31 Aethalometer instruments (Magee Scientific Inc., USA) in the 880-nm channel, recognized as the standard for BC measurement due to its strong sensitivity to BC particle absorption (Byčenkienė et al., 2013). Representativeness errors associated with comparing in situ measurements to model grid cells are expected to be smaller for relatively longer-lived aerosol species. For example, Fang et al. (2024) found that $PM_{2.5}$ shows weak intra-grid urban–rural differences at 0.5° × 0.625° resolution, implying good spatial representativeness for model–observation comparisons; BC, with an atmospheric lifetime of days to weeks, is expected to behave similarly at monthly timescales. Therefore, we use the monthly mean BC and do not introduce an additional spatial representativeness operator for surface BC in this study. We also note that the monitoring network is denser over eastern/central China and megacity clusters, and constraints are weaker where sites are sparse. As shown in Figure 3a, the posterior surface BC simulations exhibit improved consistency with the ground-based observations. Statistically, the RMSE and MAE in the four major megacity clusters decreased to 1.93 μg C m^{-3} and 1.29 μg C m^{-3}, respectively. Furthermore, the NMB is shifted to −12.00%, indicating a substantial reduction in bias.

Surface BC concentrations are closely related to BC emissions and exhibit a spatial distribution consistent with emission patterns, as discussed later. Surface BC simulations derived from the CMIP6 historical BC emissions (Figures 7c and 7d) present substantially higher concentrations than those based on both the prior and posterior BC emissions (Figures 2 and 3), especially over eastern China, central China, and SCB. This discrepancy underscores the tendency of the CMIP6 historical inventory to substantially overestimate BC emissions. Compared to the prior

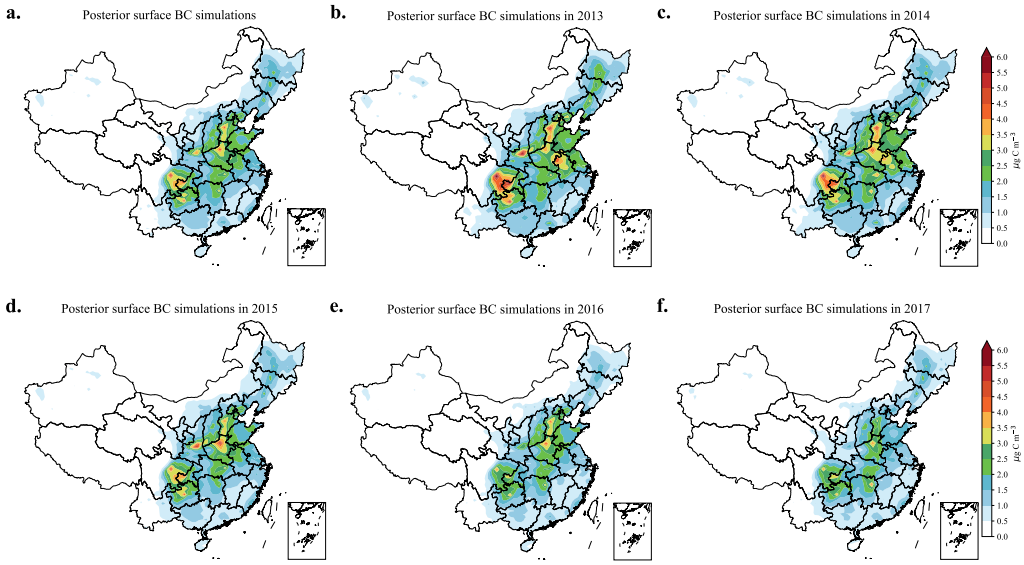

Figure 3. The spatial distribution of ground BC simulations with posterior BC emission. Panel (a) shows the average results over the entire five-year period, while Panels (b)–(f) depict the annual averages for each year from 2013 to 2017, respectively.

annual mean BC simulations (Figures 2b–2f), the posterior annual mean BC simulations (Figures 3b–3f) generally have lower surface BC concentrations and align more closely with BC observations. This alignment demonstrates the reliability and effectiveness of the emission inversion system in refining BC emission estimates.

To independently validate the effectiveness of the proposed 4DEnVar data assimilation algorithm, ground observations from Data set 2 were employed, and these were not restricted to measurements obtained solely with AE31 Aethalometer instruments. Crucially, since Data set 2 was not used in the assimilation process, it serves as an unbiased metric to verify that the inversion system has balanced prior and observational information correctly without over-fitting to Data set 1. As illustrated in Figure 4b, the simulated ground-level BC concentrations using posterior BC emission estimates exhibit a substantial improvement in agreement with Data set 2, as evidenced by significant reductions in both RMSE and MAE, regardless of the monitoring instrument type. Specifically, the RMSE decreased from 1.80 to 1.14 μg C m^{-3} and the MAE decreased from 1.27 to 0.85 μg C m^{-3}. Additionally, NMB shifts from +42.42% to −24.36%, suggesting that the prior BC emission inventory likely overestimated emissions. The relatively high negative NMB primarily arises from the use of diverse measurement instruments, each with distinct instrumental errors. Additionally, some of the BC observations from Data set 2 are not fully

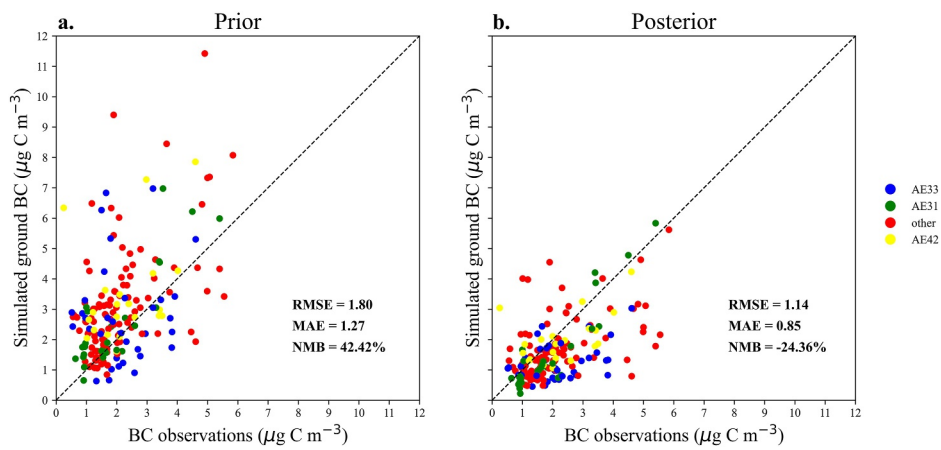

Figure 4. The scatter plot compares BC simulations with ground-based BC observations from Data set 2. Panel (a) uses prior emissions; Panel (b) uses posterior emissions. Colors indicate different monitoring instruments.

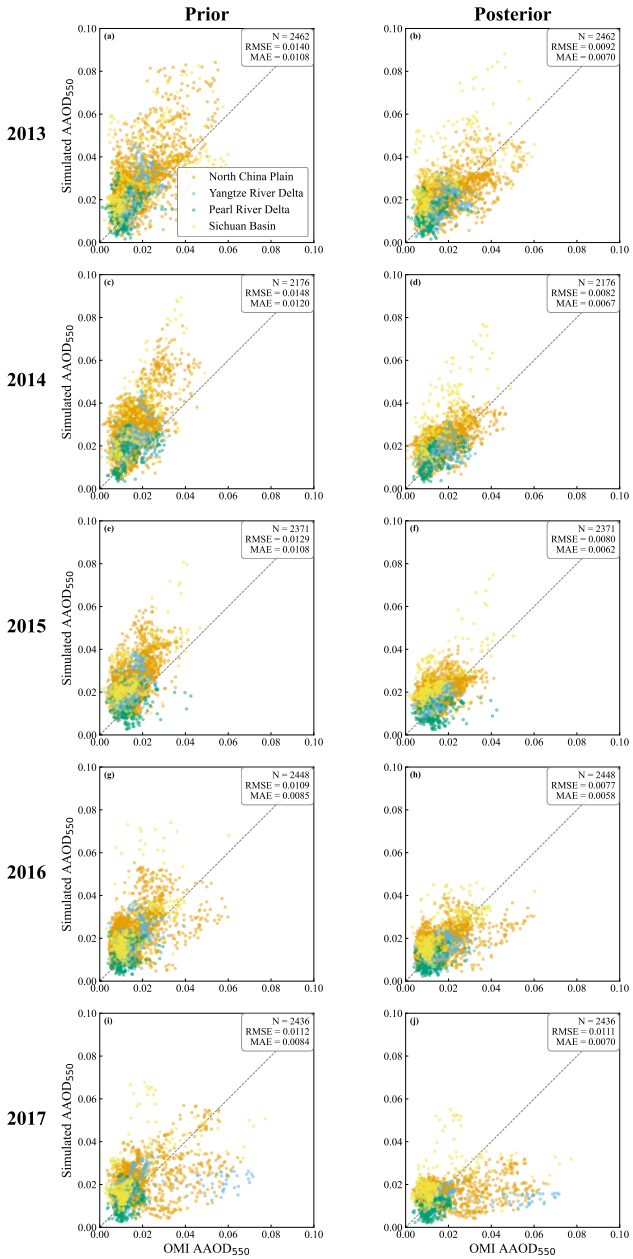

Figure 5. Scatter plots comparing OMI-retrieved AAOD550 with prior and posterior GEOS-Chem simulations for four major clusters in China during 2013–2017. Panels (a, c, e, g, i) represent the prior results from 2013 to 2017 while panels (b, d, f, h, j) represent the posterior results.

representative for comparison with the monthly mean results from GEOS-Chem simulations, as they were obtained through intermittent sampling conducted a few times per month rather than through continuous hourly measurements. BC observations from Data set 2 are mainly in urban areas, which also causes representativeness uncertainty. Since Data set 2 was not used in the assimilation, the improved agreement provides an independent validation that the posterior emissions reduce persistent emission-related inconsistencies relative to observations, while acknowledging that remaining discrepancies may arise from unresolved forward-model uncertainties. This improvement underscores the importance of observational constraints in refining BC emission estimates.

A direct comparison between satellite AAOD and simulated AAOD is not ideal or fair, as satellite AAOD integrates contributions from multiple aerosol components and has substantial retrieval uncertainty. However, changes in BC emissions are, as expected, reflected in GEOS-Chem–simulated AAOD derived from all aerosol species (Y. Jin et al., 2024), and which is comparable to the AAOD measurements. In our study, a comprehensive comparison between OMI AAOD550 and GEOS-Chem–simulated AAOD with prior BC emission or with posterior BC emission was then conducted and presented in Figure 5. The posterior simulations showed reductions in both RMSE and MAE across the four major clusters steadily. The results were generally consistent with those reported by C. Chen et al. (2019). An exception occurred in December 2017, where the improvement was marginal. This discrepancy is primarily due to the unusually high OMI AAOD550 values recorded in that month, as shown in Figure S2 in Supporting Information S1. Consequently, upon excluding the December 2017 data from the analysis, the degree of improvement aligns consistently with other years (Figure S3 in Supporting Information S1).

3.2. BC Emission Variations

BC emissions inferred from the prior, posterior, and CMIP6 historical inventories exhibit similar spatial distribution patterns but differ substantially in emission intensity across various regions. BC emissions are predominantly concentrated in NCP, YRD, SCB, Hubei province, and Hunan province as indicated by the prior, posterior, and CMIP6 historical BC emissions. Compared to the prior BC emissions shown in Figure 6a, the CMIP6 historical BC emissions (Figures 7a and 7b) exhibit a comparable spatial distribution but with consistently higher emission levels, particularly in the hotspots identified in the prior inventory. In contrast, the posterior BC emissions (Figure 6b) show the lowest overall emission levels and a notable reduction in emission intensity from 2013 to 2017. The emission increments (Figure 6c) also indicate that the posterior estimates are significantly lower than the prior, particularly in eastern China.

As illustrated in Figure 8, monthly BC emission variations follow a similar seasonal pattern, with peak emissions observed in winter and autumn and lower emissions in spring and summer. This pattern suggests that both the prior and CMIP6 historical BC emission inventories reasonably capture the temporal variations in BC emissions. In China, anthropogenic sources account for over 99% of total BC emissions (Lu et al., 2011), with residential, industrial, and transportation activities serving as the primary contributors (B. Zheng et al., 2018). The pronounced peak in BC emissions during winter in northern China is primarily driven by heating demand, as coal remains the dominant energy source during this season. Both the prior and posterior BC emissions exhibit a consistent year-by-year decreasing trend, attributable to reductions in anthropogenic emissions resulting from the implementation of the Clean Air Action. Despite this progress, the prior inventory consistently overestimates BC emissions in all

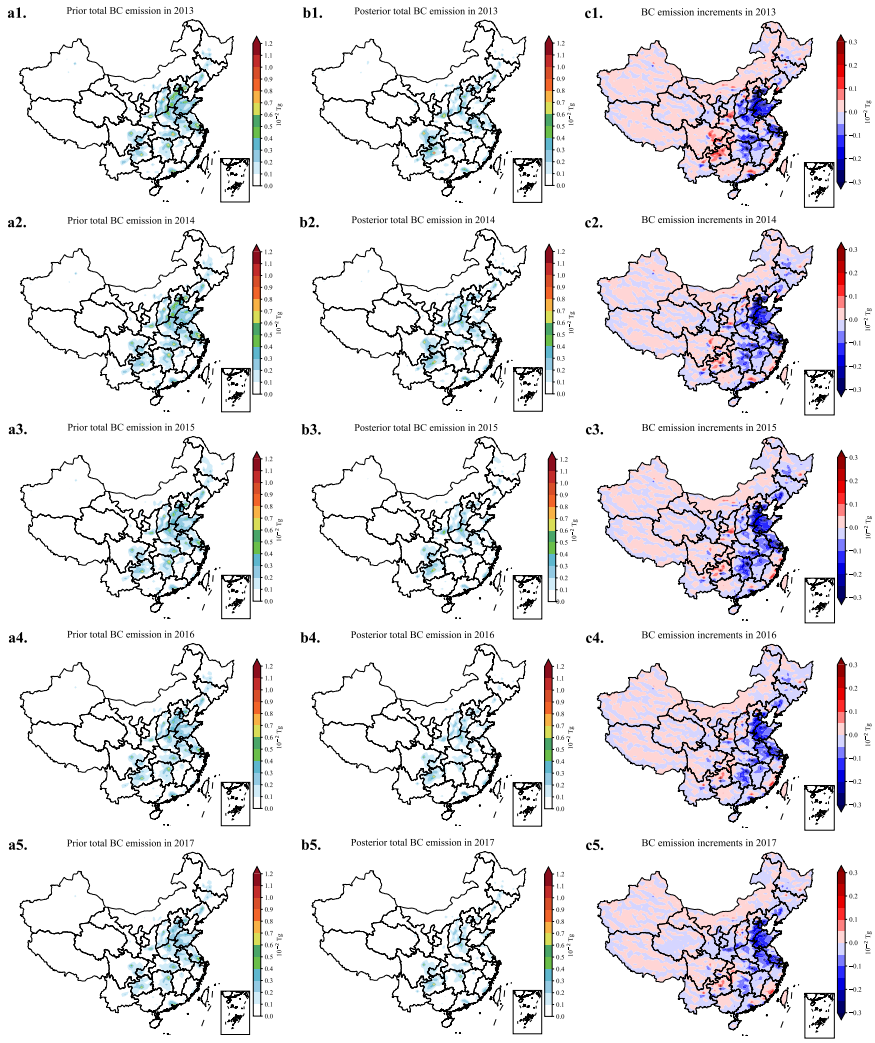

Figure 6. The spatial distribution of annual BC total emission from 2013 to 2017. Panels (a1–a5) show the prior annual BC emissions, panels (b1–b5) display the posterior annual BC emissions, and panels (c1–c5) present the differences between posterior and prior estimates.

months, while the CMIP6 historical inventory further amplifies this overestimation. Notably, the posterior BC emissions reveal an interesting seasonal peak in March, with peak values first decreasing and then slightly increasing over the study period. This phenomenon may be linked to agricultural practices such as straw and biomass burning, which are most prevalent in March and October in China (J. Zhang et al., 2019).

Due to the implementation of the Clean Air Action, annual total BC emissions have consistently declined, as shown by both the prior and posterior BC emissions in Figure 9a. Statistically, the prior annual total BC emissions are estimated to decrease from 1.68 Tg in 2013 to 1.21 Tg in 2017, representing a reduction of 28.0%. The posterior BC emission estimates imply lower BC emissions than the prior, with annual total emissions decreasing from 1.24 Tg in 2013 to 0.89 Tg in 2017, corresponding to a reduction of 28.2%. Note that while the inversion is robust for the major emission clusters that drive the national trend, the estimates for Western China rely primarily on the prior inventory due to limited observational constraints, though their impact on the national total is minimal. This finding aligns with studies (Y. Zheng et al., 2017; Q. Zhang & Geng, 2019; H. Zhou et al., 2024) showing accelerated air quality improvements during this period, but provides the first BC-specific quantification based on extensive ground observations. Notably, the CMIP6 historical BC emission inventory tends to overestimate actual BC emissions by nearly a factor of two. This overestimation is likely to extend to the CMIP6

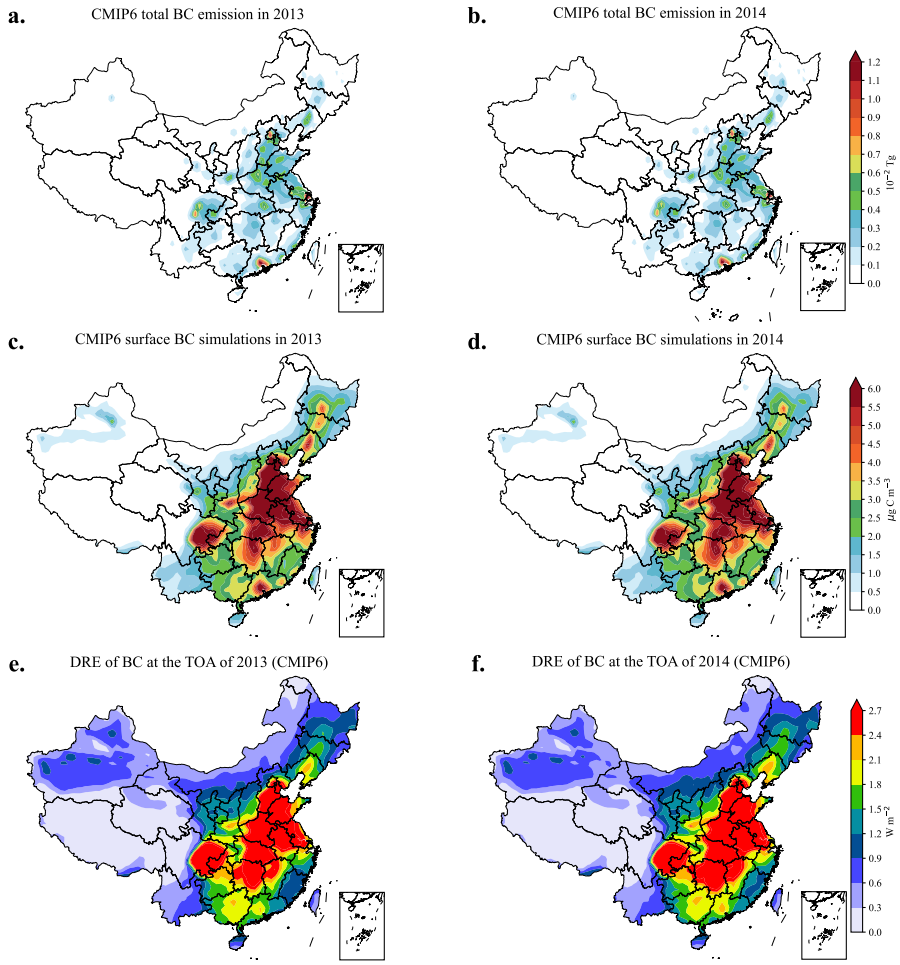

Figure 7. The spatial distributions of BC emissions, surface concentrations, and DRE at the TOA simulated using CMIP6 historical inventory in 2013 and 2014. Panels (a) and (b) present the total BC emissions, panels (c) and (d) depict the surface BC concentrations, and panels (e) and (f) illustrate the BC DRE at the TOA.

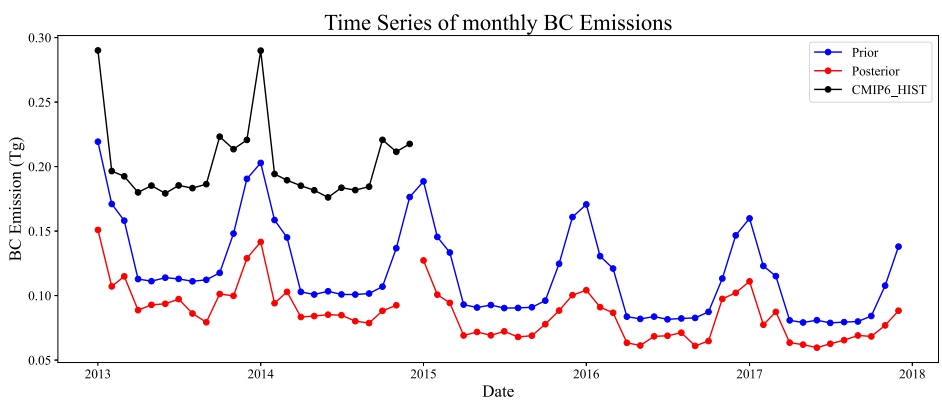

Figure 8. The temporal variations of monthly BC emissions are depicted, with blue, red, and black dots representing emissions estimated from Prior, Posterior, and CMIP6 historical inventories, respectively. The posterior emission for December 2014 is not shown due to a lack of observations for data assimilation, and the CMIP6 historical inventory is only updated through 2014.

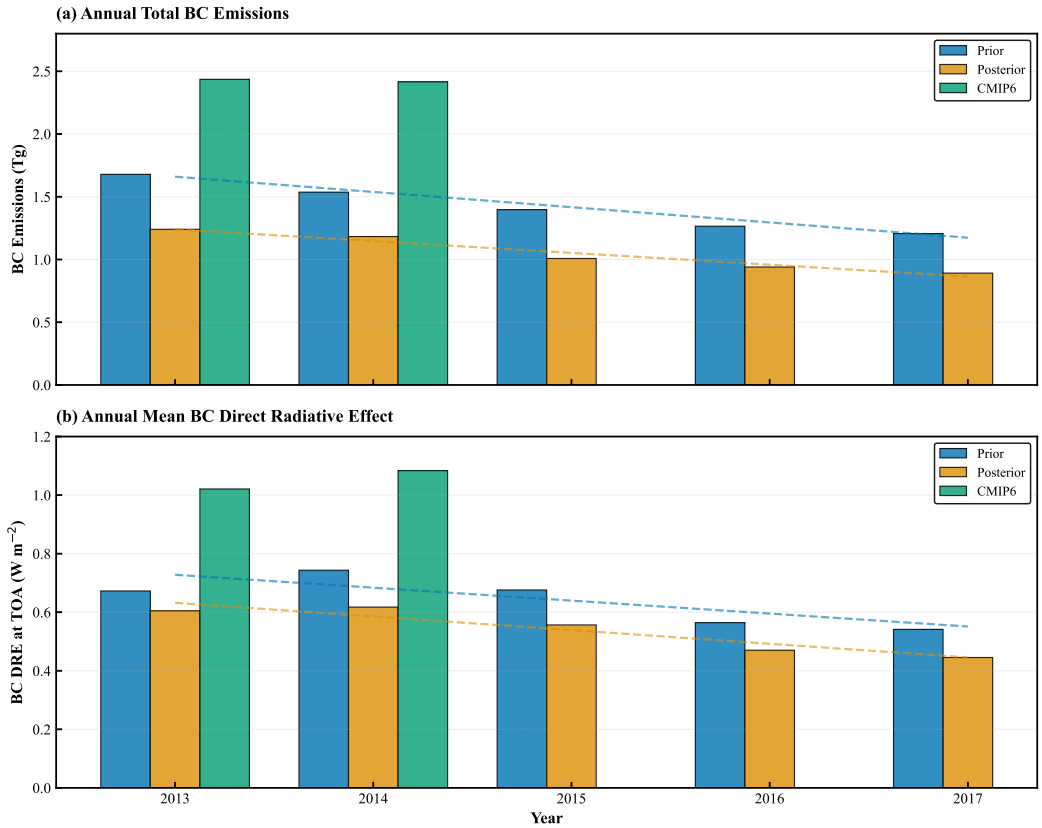

Figure 9. The annual BC total emissions and BC direct radiative effect at the TOA from 2013 to 2017. The blue, orange, and green colors represent prior, posterior, and CMIP6, respectively. Note that the posterior emission for December 2014 utilizes the corresponding month's prior emission, and the CMIP6 historical inventory is only available up to 2014.

future BC emissions, which could lead to misinterpretations of future BC variations and their corresponding radiative effects on climate feedback.

Both prior and posterior emission estimates demonstrate a marked decline in BC emissions across all regions during the study period, reflecting the effectiveness of the Clean Air Action. Figure 10 presents the temporal trends of annual total BC emissions from 2013 to 2017 over four major regions of China, based on both prior and posterior estimates. The posterior estimates, depicted by the red solid line, consistently indicates lower emission levels compared to the prior estimates (blue solid line) in NCP, YRD and PRD. Among these regions, NCP shows the largest emission amount and reduction, consistent with its intensive industrial and widespread residential coal use, particularly before 2013. YRD, a more economically advanced region with earlier industrial restructuring, exhibited the second-largest reduction in BC emissions, despite starting from a relatively lower emission level. The relatively smaller absolute reductions observed in PRD could be linked to its distinct emission structure, dominated by transportation activities rather than industrial, which may be less responsive to policy interventions. In addition, as a coastal region influenced by the subtropical monsoon, PRD generally experiences stronger ventilation and more frequent precipitation than northern China, which can enhance pollutant dispersion and wet removal and may partially contribute to the relatively modest reduction inferred here (Lo et al., 2006). The most significant divergence between the prior and posterior estimates is observed in SCB, where the posterior trend indicates a much steeper decline in emissions. This suggests that prior estimates may have underestimated the effectiveness of pollution control policies in this region. The SCB posterior–prior contrast is consistent with the strong decline observed at the available SCB site, but it should also be noted that the SCB features complex terrain and sparse observational coverage, which can lead to larger inversion errors in this region. These findings reflect the efficacy of aggressive air pollution control measures implemented following the Air Pollution Prevention and Control Action Plan, which targeted residential coal use, industrial emissions, and vehicular pollution.

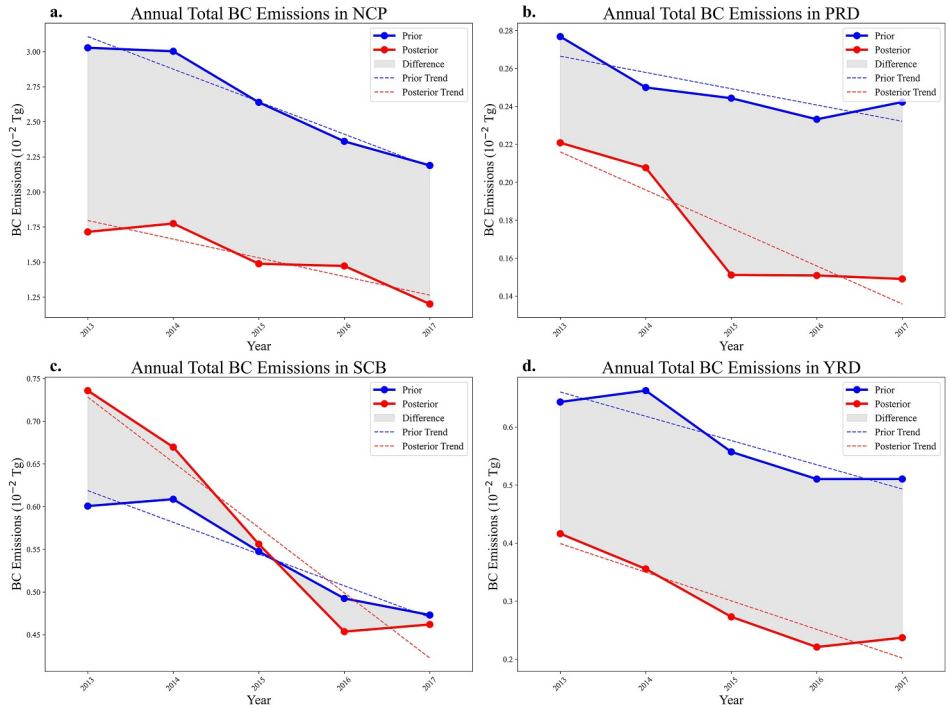

Figure 10. The annual BC total emissions for the four megacity clusters from 2013 to 2017. The blue and red solid lines represent the prior and posterior BC inventories, respectively, while the dashed line indicates their trend.

3.3. Radiative Effect

This section provides a more accurate assessment of the climatic impact of BC through its DRE at the TOA, highlighting the limitations of existing inventories such as CMIP6 historical inventory. The DRE of BC at the TOA is quantified using the clear-sky shortwave radiation outputs from the RRTMG. The DRE is determined as the difference in TOA shortwave radiative flux between simulations with and without BC aerosols, while maintaining consistent meteorological and surface conditions. This methodology isolates BC's contribution to the radiative balance, offering crucial insights into its role in modulating Earth's energy budget. BC exerts a positive DRE at the TOA, signifying its contribution to net atmospheric warming. This warming arises from BC's strong absorption of solar radiation in the shortwave spectrum, converting it into heat and consequently impacting regional and global climate dynamics. It is important to note that the comparison below is performed entirely within the GEOS-Chem + RRTMG framework, using identical model physics and optical parameterizations but different BC emission inventories (posterior, MEIC, and CMIP6 historical). Therefore, the difference represents how the simulated clear-sky TOA shortwave DRE responds to alternative emission inputs within this model, rather than a multi-model evaluation of CMIP6 effective radiative forcing. Because our DRE estimates exclude cloud-radiative adjustments, and BC forcing also depends on aerosol optical properties, mixing state, vertical distribution, and cloud interactions.

The spatial distributions of prior and posterior BC DRE at the TOA (Figure 11) closely resemble the corresponding patterns of surface BC concentrations (Figures 2 and 3), reflecting the strong linkage between emissions and radiative forcing. Notably, the prior BC DRE (left column of Figure 11) exhibits higher values than the posterior DRE (right column of Figure 11), with particularly pronounced differences over NCP, central China, and SCB. These discrepancies are indicative of an overestimation of BC emissions in the prior inventory, which is effectively corrected in the posterior fields through the incorporation of observational constraints. In contrast, simulations based on the CMIP6 historical inventory (Figures 7e and 7f) produce even greater BC DRE values at the TOA, particularly over southern and central China, attributable to the higher BC emission estimates in the CMIP6 historical inventory. It should be noted that we restrict the comparison to the 2013–2014 prior and posterior estimates when evaluating the CMIP6 DRE, because the CMIP6 historical emissions inventory is only

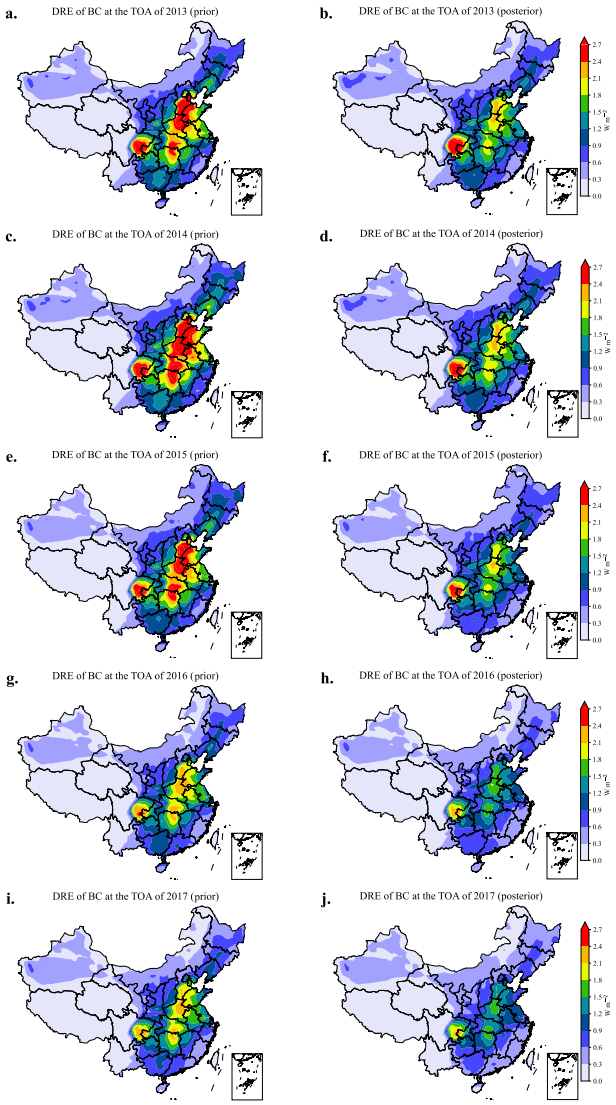

Figure 11. The spatial distribution of annual averaged BC DRE at the TOA from 2013 to 2017. Panels (a, c, e, g, i) show DRE simulations based on the prior emission inventory, while panels (b, d, f, h, j) illustrate DRE simulations using the posterior BC emission inventory.

available up to 2014. This overestimation highlights a critical limitation of the CMIP6 inventory and underscores the need for caution in using CMIP6 for future projections of BC emissions and associated climate impacts.

Temporal trends in prior and posterior BC DRE at the TOA during the Clean Air Action period, alongside comparisons with CMIP6 estimates, are presented in Figure 9b. The prior annual mean BC DRE demonstrates a clear decline, decreasing from 0.67 W m^{-2} in 2013 to 0.54 W m^{-2} in 2017, consistent with reductions in BC emissions. Similarly, the posterior annual mean BC DRE shows a steady decrease, from 0.60 W m^{-2} in 2013 to 0.45 W m^{-2} in 2017, but is significantly lower than the prior. In contrast, the annual mean BC DRE derived from CMIP6 historical emissions was significantly higher, reaching 1.02 W m^{-2} in 2013 and 1.08 W m^{-2} in 2014. This discrepancy suggests substantial overestimations of BC emissions and radiative effects in CMIP6, which could mislead future climate projections. Although the CMIP6 historical inventory is not available beyond 2014, the consistent downward trends in prior and posterior BC DRE observed between 2013 and 2014 are not reflected in the CMIP6. These advancements are critical for capturing the temporal and spatial variability of BC's radiative effects, thereby enhancing the accuracy of climate models and informing more effective policy decisions.

4. Conclusions

This study presents the first application of nationwide ground-based BC observations in emission inversion during China's Clean Air Action, using a 4DEnVar data assimilation approach. The posterior BC emission estimates significantly improve the model's ability to reproduce the spatiotemporal variability of BC concentrations, resulting in a 36.7% reduction in RMSE evaluation compared with the prior simulation. Our emission inversion revealed that the commonly used bottom-up inventories (e.g., MEIC) overestimate China's total BC emissions by 36.7%, with the overestimation reaching up to 80.6% in NCP (averaged over 2013–2017). The results also underscore the effectiveness of the Clean Air Action in reducing anthropogenic BC emissions by 28.1% during 2013–2017, with substantial reductions over major emission hotspots such as NCP (a reduction of 30.0%).

The climate implications of our revised BC estimates are substantial. The 18.7% overestimation in DRE from MEIC-based simulations, and the even more pronounced 75.7% overestimation from CMIP6 historical inventories, suggest that current climate models may be significantly misrepresenting BC's contribution to regional warming. This has cascading effects on climate projections, as overestimated BC forcing could lead to incorrect attribution of historical warming trends and flawed predictions of future climate responses to emission changes. Given BC's role as a short-lived climate forcer with strong regional effects, accurate emission estimates are crucial for understanding regional climate dynamics.

Conflict of Interest

The authors declare no conflicts of interest relevant to this study.

Data Availability Statement

The emission inversion methodology is in the Python environment and is archived on Zenodo (J. Jin, 2022). The ground BC observations are publicly available via Zenodo (Fang, 2026). The MEIC emission inventory for BC is available at http://meicmodel.org.cn.

Acknowledgments
This work was supported by the National Natural Science Foundation of China (Grants 42475150 and 42021004).

References

Andreae, M., & Rosenfeld, D. (2008). Aerosol–cloud–precipitation interactions. Part 1. The nature and sources of cloud-active aerosols. *Earth-Science Reviews*, *89*(1–2), 13–41. https://doi.org/10.1016/j.earscirev.2008.03.001

Babyale, S. R., Mead, J., Calhoun, D., & Azike, P. O. (2025). Model error covariance estimation for weak constraint variational data assimilation. *SIAM/ASA Journal on Uncertainty Quantification*, *13*(4), 1828–1861. https://doi.org/10.1137/24M1695889

Bond, T. C., Streets, D. G., Yarber, K. F., Nelson, S. M., Woo, J.-H., & Klimont, Z. (2004). A technology-based global inventory of black and organic carbon emissions from combustion. *Journal of Geophysical Research*, *109*(D14). https://doi.org/10.1029/2003JD003697

Byčenkienė, S., Ulevicius, V., Dudoitis, V., & Pauraitė, J. (2013). Identification and characterization of black carbon aerosol sources in the east baltic region. *Advances in Meteorology*, *2013*, 1–11. https://doi.org/10.1155/2013/380614

Cao, G., Zhang, X., & Zheng, F. (2006). Inventory of black carbon and organic carbon emissions from China. *Atmospheric Environment*, *40*(34), 6516–6527. https://doi.org/10.1016/j.atmosenv.2006.05.070

Cesnulyte, V., Lindfors, A. V., Pitkänen, M. R. A., Lehtinen, K. E. J., Morcrette, J.-J., & Arola, A. (2014). Comparing ecmwf aod with aeronet observations at visible and uv wavelengths. *Atmospheric Chemistry and Physics*, *14*(2), 593–608. https://doi.org/10.5194/acp-14-593-2014

Chen, C., Dubovik, O., Henze, D. K., Chin, M., Lapyonok, T., Schuster, G. L., et al. (2019). Constraining global aerosol emissions using polder/parasol satellite remote sensing observations. *Atmospheric Chemistry and Physics*, *19*(23), 14585–14606. https://doi.org/10.5194/acp-19-14585-2019

Cooke, W. F., Liousse, C., Cachier, H., & Feichter, J. (1999). Construction of a 1° × 1° fossil fuel emission data set for carbonaceous aerosol and implementation and radiative impact in the echam4 model. *Journal of Geophysical Research*, *104*(D18), 22137–22162. https://doi.org/10.1029/1999JD900187

Dentener, F., Hall, B., Smith, C., Ahn, J., Collins, W., Jones, C., et al. (2021). Annex III: Tables of historical and projected well-mixed greenhouse gas mixing ratios and effective radiative forcing of all climate forcers. In V. Masson-Delmotte, et al. (Eds.), *Climate change 2021: The physical science basis. contribution of working group i to the sixth assessment report of the intergovernmental panel on climate change* (pp. 2139–2152). Cambridge University Press.https://doi.org/10.1017/9781009157896.017

Ding, A. J., Huang, X., Nie, W., Sun, J. N., Kerminen, V.-M., Petäjä, T., et al. (2016). Enhanced haze pollution by black carbon in megacities in China. *Geophysical Research Letters*, *43*(6), 2873–2879. https://doi.org/10.1002/2016GL067745

Eyring, V., Bony, S., Meehl, G. A., Senior, C. A., Stevens, B., Stouffer, R. J., & Taylor, K. E. (2016). Overview of the coupled model intercomparison project phase 6 (cmip6) experimental design and organization. *Geoscientific Model Development*, *9*(5), 1937–1958. https://doi.org/10.5194/gmd-9-1937-2016

Fang, L. (2026). The ground bc observations. *Zenodo*. https://doi.org/10.5281/zenodo.18192098

Fang, L., Jin, J., Segers, A., Li, K., Xia, J., Han, W., et al. (2024). Observational operator for fair model evaluation with ground no_2 measurements. *Geoscientific Model Development*, *17*(22), 8267–8282. https://doi.org/10.5194/gmd-17-8267-2024

Feng, L., Smith, S. J., Braun, C., Crippa, M., Gidden, M. J., Hoesly, R., et al. (2020). The generation of gridded emissions data for cmip6. *Geoscientific Model Development*, *13*(2), 461–482. https://doi.org/10.5194/gmd-13-461-2020

Gelaro, R., McCarty, W., Suárez, M. J., Todling, R., Molod, A., Takacs, L., et al. (2017). The modern-era retrospective analysis for research and applications, version 2 (merra-2). *Journal of Climate*, *30*(14), 5419–5454. https://doi.org/10.1175/JCLI-D-16-0758.1

Giglio, L., Randerson, J. T., & van der Werf, G. R. (2013). Analysis of daily, monthly, and annual burned area using the fourth-generation global fire emissions database (gfed4). *Journal of Geophysical Research: Biogeosciences*, *118*(1), 317–328. https://doi.org/10.1002/jgrg.20042

Guo, B., Wang, Y., Zhang, X., Che, H., Ming, J., & Yi, Z. (2020). Long-term variation of black carbon aerosol in China based on revised aethalometer monitoring data. *Atmosphere*, *11*(7), 684. https://doi.org/10.3390/atmos11070684

Hakami, A., Henze, D. K., Seinfeld, J. H., Chai, T., Tang, Y., Carmichael, G. R., & Sandu, A. (2005). Adjoint inverse modeling of black carbon during the asian pacific regional aerosol characterization experiment. *Journal of Geophysical Research*, *110*(D14). https://doi.org/10.1029/2004JD005671

Heald, C. L., Ridley, D. A., Kroll, J. H., Barrett, S. R. H., Cady-Pereira, K. E., Alvarado, M. J., & Holmes, C. D. (2014). Contrasting the direct radiative effect and direct radiative forcing of aerosols. *Atmospheric Chemistry and Physics*, *14*(11), 5513–5527. https://doi.org/10.5194/acp-14-5513-2014

Hoesly, R. M., Smith, S. J., Feng, L., Klimont, Z., Janssens-Maenhout, G., Pitkanen, T., et al. (2018). Historical (1750–2014) anthropogenic emissions of reactive gases and aerosols from the community emissions data system (ceds). *Geoscientific Model Development*, *11*(1), 369–408. https://doi.org/10.5194/gmd-11-369-2018

Huneeus, N., Boucher, O., & Chevallier, F. (2013). Atmospheric inversion of so_2 and primary aerosol emissions for the year 2010. *Atmospheric Chemistry and Physics*, *13*(13), 6555–6573. https://doi.org/10.5194/acp-13-6555-2013

Iacono, M. J., Delamere, J. S., Mlawer, E. J., Shephard, M. W., Clough, S. A., & Collins, W. D. (2008). Radiative forcing by long-lived greenhouse gases: Calculations with the aer radiative transfer models. *Journal of Geophysical Research*, *113*(D13). https://doi.org/10.1029/2008JD009944

Jia, M., Evangeliou, N., Eckhardt, S., Huang, X., Gao, J., Ding, A., & Stohl, A. (2021). Black carbon emission reduction due to covid-19 lockdown in China. *Geophysical Research Letters*, *48*(8), e2021GL093243. https://doi.org/10.1029/2021GL093243

Jin, J. (2022). 4denvar code for ammonia emission inversion. *Zenodo*. https://doi.org/10.5281/zenodo.7015397

Jin, J., Fang, L., Li, B., Liao, H., Wang, Y., Han, W., et al. (2023). 4denvar-based inversion system for ammonia emission estimation in China through assimilating iasi ammonia retrievals. *Environmental Research Letters*, *18*(3), 34005. https://doi.org/10.1088/1748-9326/acb835

Jin, J., Lin, H. X., Segers, A., Xie, Y., & Heemink, A. (2019). Machine learning for observation bias correction with application to dust storm data assimilation. *Atmospheric Chemistry and Physics*, *19*(15), 10009–10026. https://doi.org/10.5194/acp-19-10009-2019

Jin, J., Segers, A., Heemink, A., Yoshida, M., Han, W., & Lin, H.-X. (2019). Dust emission inversion using himawari-8 aods over east Asia: An extreme dust event in may 2017. *Journal of Advances in Modeling Earth Systems*, *11*(2), 446–467. https://doi.org/10.1029/2018MS001491

Jin, Y., Liu, Y., Lu, X., Chen, X., Shen, A., Wang, H., et al. (2024). Measurement report: Assessing the impacts of emission uncertainty on aerosol optical properties and radiative forcing from biomass burning in peninsular southeast Asia. *Atmospheric Chemistry and Physics*, *24*(1), 367–395. https://doi.org/10.5194/acp-24-367-2024

Karavalakis, G., Short, D., Vu, D., Villela, M., Asa-Awuku, A., & Durbin, T. D. (2014). Evaluating the regulated emissions, air toxics, ultrafine particles, and black carbon from si-pfi and si-di vehicles operating on different ethanol and iso-butanol blends. *Fuel*, *128*, 410–421. https://doi.org/10.1016/j.fuel.2014.03.016

Kinne, S., Schulz, M., Textor, C., Guibert, S., Balkanski, Y., Bauer, S. E., et al. (2006). An aerocom initial assessment – Optical properties in aerosol component modules of global models. *Atmospheric Chemistry and Physics*, *6*(7), 1815–1834. https://doi.org/10.5194/acp-6-1815-2006

Li, M., Liu, H., Geng, G., Hong, C., Liu, F., Song, Y., et al. (2017). Anthropogenic emission inventories in China: A review. *National Science Review*, *4*(6), 834–866. https://doi.org/10.1093/nsr/nwx150

Liousse, C., Cachier, H., & Jennings, S. (1993). Optical and thermal measurements of black carbon aerosol content in different environments: Variation of the specific attenuation cross-section, sigma (σ). Atmospheric Environment. Part A. *General Topics*, *27*(8), 1203–1211. https://doi.org/10.1016/0960-1686(93)90246-U

Liu, C., Xiao, Q., & Wang, B. (2008). An ensemble-based four-dimensional variational data assimilation scheme. part i: Technical formulation and preliminary test. *Monthly Weather Review*, *136*(9), 3363–3373. https://doi.org/10.1175/2008MWR2312.1

Lo, J. C. F., Lau, A. K. H., Fung, J. C. H., & Chen, F. (2006). Investigation of enhanced cross-city transport and trapping of air pollutants by coastal and urban land-sea breeze circulations. *Journal of Geophysical Research*, *111*(D14). https://doi.org/10.1029/2005JD006837

Lu, Z., Zhang, Q., & Streets, D. G. (2011). Sulfur dioxide and primary carbonaceous aerosol emissions in China and India, 1996–2010. *Atmospheric Chemistry and Physics*, *11*(18), 9839–9864. https://doi.org/10.5194/acp-11-9839-2011

McCormick, R. A., & Ludwig, J. H. (1967). Climate modification by atmospheric aerosols. *Science*, *156*(3780), 1358–1359. https://doi.org/10.1126/science.156.3780.1358

Menon, S., Hansen, J., Nazarenko, L., & Luo, Y. (2002). Climate effects of black carbon aerosols in China and India. *Science*, *297*(5590), 2250–2253. https://doi.org/10.1126/science.1075159

Paliwal, U., Sharma, M., & Burkhart, J. F. (2016). Monthly and spatially resolved black carbon emission inventory of India: Uncertainty analysis. *Atmospheric Chemistry and Physics*, *16*(19), 12457–12476. https://doi.org/10.5194/acp-16-12457-2016

Park, R. J., Jacob, D. J., Chin, M., & Martin, R. V. (2003). Sources of carbonaceous aerosols over the United States and implications for natural visibility. *Journal of Geophysical Research*, *108*(D12). https://doi.org/10.1029/2002JD003190

Park, R. J., Jacob, D. J., Field, B. D., Yantosca, R. M., & Chin, M. (2004). Natural and transboundary pollution influences on sulfate-nitrate-ammonium aerosols in the United States: Implications for policy. *Journal of Geophysical Research*, *109*(D15). https://doi.org/10.1029/2003JD004473

Park, R. J., Jacob, D. J., Palmer, P. I., Clarke, A. D., Weber, R. J., Zondlo, M. A., et al. (2005). Export efficiency of black carbon aerosol in continental outflow: Global implications. *Journal of Geophysical Research*, *110*(D11). https://doi.org/10.1029/2004JD005432

Penner, J., Eddleman, H., & Novakov, T. (1993). Towards the development of a global inventory for black carbon emissions. Atmospheric Environment. Part A. *General Topics*, *27*(8), 1277–1295. https://doi.org/10.1016/0960-1686(93)90255-W

Ramanathan, V., & Carmichael, G. (2008). Global and regional climate changes due to black carbon. *Nature Geoscience*, *1*(4), 221–227. https://doi.org/10.1038/ngeo156

Randles, C. A., da Silva, A. M., Buchard, V., Colarco, P. R., Darmenov, A., Govindaraju, R., et al. (2017). The merra-2 aerosol reanalysis, 1980 onward. Part I: System description and data assimilation evaluation. *Journal of Climate*, *30*(17), 6823–6850. https://doi.org/10.1175/JCLI-D-16-0609.1

Rosenfeld, D. (2000). Suppression of rain and snow by urban and industrial air pollution. *Science*, *287*(5459), 1793–1796. https://doi.org/10.1126/science.287.5459.1793

Schulz, M., Textor, C., Kinne, S., Balkanski, Y., Bauer, S., Berntsen, T., et al. (2006). Radiative forcing by aerosols as derived from the aerocom present-day and pre-industrial simulations. *Atmospheric Chemistry and Physics*, *6*(12), 5225–5246. https://doi.org/10.5194/acp-6-5225-2006

Schutgens, N., Dubovik, O., Hasekamp, O., Torres, O., Jethva, H., Leonard, P. J. T., et al. (2021). Aerocom and aerosat aaod and ssa study – Part 1: Evaluation and intercomparison of satellite measurements. *Atmospheric Chemistry and Physics*, *21*(9), 6895–6917. https://doi.org/10.5194/acp-21-6895-2021

State Council of the People's Republic of China. (2018). China achieves desired results in clean air action plan: Official. Retrieved from https://english.www.gov.cn/state_council/ministries/2018/01/31/content_281476032072026.htm

Sun, J., Wang, Z., Zhou, W., Xie, C., Wu, C., Chen, C., et al. (2022). Measurement report: Long-term changes in black carbon and aerosol optical properties from 2012 to 2020 in beijing, China. *Atmospheric Chemistry and Physics*, *22*(1), 561–575. https://doi.org/10.5194/acp-22-561-2022

Tao, S., Ru, M., Du, W., Zhu, X., Zhong, Q., Li, B., et al. (2018). Quantifying the rural residential energy transition in China from 1992 to 2012 through a representative national survey. *Nature Energy*, *3*(7), 567–573. https://doi.org/10.1038/s41560-018-0158-4

The International GEOS-Chem User Community. (2022). Geoschem/gcclassic: Geos-chem 13.4.0. *Zenodo*. https://doi.org/10.5281/zenodo.6511970

Torres, O. O. (2008). OMI/aura near UV aerosol optical depth and single scattering Albedo L3 1 day 1.0 degree × 1.0 degree V3. *NASA Goddard Space Flight Center: Goddard Earth Sciences Data and Information Services Center (GES DISC)*. https://doi.org/10.5067/Aura/OMI/DATA3003

Wang, J., Su, H., Wei, C., Zheng, G., Wang, J., Su, T., et al. (2023). Black-carbon-induced regime transition of boundary layer development strongly amplifies severe haze. *One Earth*, *6*(6), 751–759. https://doi.org/10.1016/j.oneear.2023.05.010

Wang, P., Wang, H., Wang, Y. Q., Zhang, X. Y., Gong, S. L., Xue, M., et al. (2016). Inverse modeling of black carbon emissions over China using ensemble data assimilation. *Atmospheric Chemistry and Physics*, *16*(2), 989–1002. https://doi.org/10.5194/acp-16-989-2016

Wang, X., Heald, C. L., Sedlacek, A. J., de Sá, S. S., Martin, S. T., Alexander, M. L., et al. (2016). Deriving brown carbon from multiwavelength absorption measurements: Method and application to aeronet and aethalometer observations. *Atmospheric Chemistry and Physics*, *16*(19), 12733–12752. https://doi.org/10.5194/acp-16-12733-2016

Xu, H., Ren, Y., Zhang, W., Meng, W., Yun, X., Yu, X., et al. (2021). Updated global black carbon emissions from 1960 to 2017: Improvements, trends, and drivers. *Environmental Science & Technology*, *55*(12), 7869–7879. https://doi.org/10.1021/acs.est.1c03117

Xu, X., Wang, J., Henze, D. K., Qu, W., & Kopacz, M. (2013). Correction to "constraints on aerosol sources using geos-chem adjoint and modis radiances, and evaluation with multisensor (omi, misr) data". *Journal of Geophysical Research: Atmospheres*, *118*(17), 10139. https://doi.org/10.1002/jgrd.50784

Zhang, J., Yang, X., Tu, X., N, K., & L, X. (2019). Spatio-temporal change of straw burning fire points in field of China from 2014 to 2018. *Transactions of the Chinese Society of Agricultural Engineering*, *35*(19), 191–199. https://doi.org/10.11975/j.issn.1002-6819.2019.19.023

Zhang, L., Henze, D. K., Grell, G. A., Carmichael, G. R., Bousserez, N., Zhang, Q., et al. (2015). Constraining black carbon aerosol over Asia using omi aerosol absorption optical depth and the adjoint of geos-chem. *Atmospheric Chemistry and Physics*, *15*(18), 10281–10308. https://doi.org/10.5194/acp-15-10281-2015

Zhang, Q., & Geng, G. (2019). Impact of clean air action on pm2. 5 pollution in China. *Science China Earth Sciences*, *62*(12), 1845–1846. https://doi.org/10.1007/s11430-019-9531-4

Zhang, W., Lu, Z., Xu, Y., Wang, C., Gu, Y., Xu, H., & Streets, D. G. (2018). Black carbon emissions from biomass and coal in rural China. *Atmospheric Environment*, *176*, 158–170. https://doi.org/10.1016/j.atmosenv.2017.12.029

Zhang, Y., Li, Y., Guo, J., Wang, Y., Chen, D., & Chen, H. (2019). The climatology and trend of black carbon in China from 12-year ground observations. *Climate Dynamics*, *53*(9–10), 5881–5892. https://doi.org/10.1007/s00382-019-04903-0

Zhao, W., Zhao, Y., Zheng, Y., Chen, D., Xin, J., Li, K., et al. (2024). Long-term variability in black carbon emissions constrained by gap-filled absorption aerosol optical depth and associated premature mortality in China. *Atmospheric Chemistry and Physics*, *24*(11), 6593–6612. https://doi.org/10.5194/acp-24-6593-2024

Zheng, B., Tong, D., Li, M., Liu, F., Hong, C., Geng, G., et al. (2018). Trends in china's anthropogenic emissions since 2010 as the consequence of clean air actions. *Atmospheric Chemistry and Physics*, *18*(19), 14095–14111. https://doi.org/10.5194/acp-18-14095-2018

Zheng, Y., Xue, T., Zhang, Q., Geng, G., Tong, D., Li, X., & He, K. (2017). Air quality improvements and health benefits from china's clean air action since 2013. *Environmental Research Letters*, *12*(11), 114020. https://doi.org/10.1088/1748-9326/aa8a32

Zhou, H., Yue, X., Dai, H., Geng, G., Yuan, W., Chen, J., et al. (2024). Recovery of ecosystem productivity in China due to the clean air action plan. *Nature Geoscience*, *17*(12), 1233–1239. https://doi.org/10.1038/s41561-024-01586-z

References From the Supporting Information

Chen, W., Tian, H., & Qin, K. (2019). Black carbon aerosol in the industrial city of xuzhou, China: Temporal characteristics and source appointment. *Aerosol and Air Quality Research*, *19*(4), 794–811. https://doi.org/10.4209/aaqr.2018.07.0245

Ding, C., Cheng, W., Dui, W., Jian, L., Lang, S., Tian-lin, S., et al. (2018). Comparative study on the characteristics of black carbon aerosol in urban and suburban areas of shenzhen. *China Environmental Science*, *38*(5), 1653. Retrieved from http://www.zghjkx.com.cn/EN/abstract/article_15682.shtml

Jing, A., Zhu, B., Wang, H., Yu, X., An, J., & Kang, H. (2019). Source apportionment of black carbon in different seasons in the northern suburb of nanjing, China. *Atmospheric Environment*, *201*, 190–200. https://doi.org/10.1016/j.atmosenv.2018.12.060

Wei, C., Wang, M. H., Fu, Q. Y., Dai, C., Huang, R., & Bao, Q. (2020). Temporal characteristics and potential sources of black carbon in megacity shanghai, China. *Journal of Geophysical Research: Atmospheres*, *125*(9), e2019JD031827. https://doi.org/10.1029/2019JD031827

Zhou, B., Wang, Q., Zhou, Q., Zhang, Z., Wang, G., Fang, N., et al. (2018). Seasonal characteristics of black carbon aerosol and its potential source regions in baoji, China. *Aerosol and Air Quality Research*, *18*(2), 397–406. https://doi.org/10.4209/aaqr.2017.02.0070